Section 2
ADVANCED TECHNOLOGY DEVELOPMENTS

2.A   High-Power Laser Interferometry

Central to the uniformity issue is the need to determine the factors that control the target-plane intensity distribution of the 24 OMEGA UV laser beams. The extent to which they can be controlled will determine overall target irradiation uniformity. Wave-front measurement and analysis techniques have generated accurate near-field intensity and phase, and target-plane intensity distributions of individual laser beams. Direct-phase measurements have uncovered phase structures in the UV beams that are responsible for hot spots on target. They have revealed the relative importance of the nonuniformity sources that affect the intensity modulation on the target surface. High-power laser interferometry is a key technological advancement in solid-state laser development and in the understanding of laser-beam focusability.

Phase-Front Recording and Reconstruction

Expressions describing the interference between test and reference beams show the means by which the phase is extracted from a high-carrier-frequency interferogram. Let the test-beam wave and reference wave be represented by

$$T(x,y)\cos\left[-\omega t + kx\sin(\alpha/2) + ky\sin(\gamma/2) + \psi(x,y)\right] \quad \text{(test)} \tag{1}$$
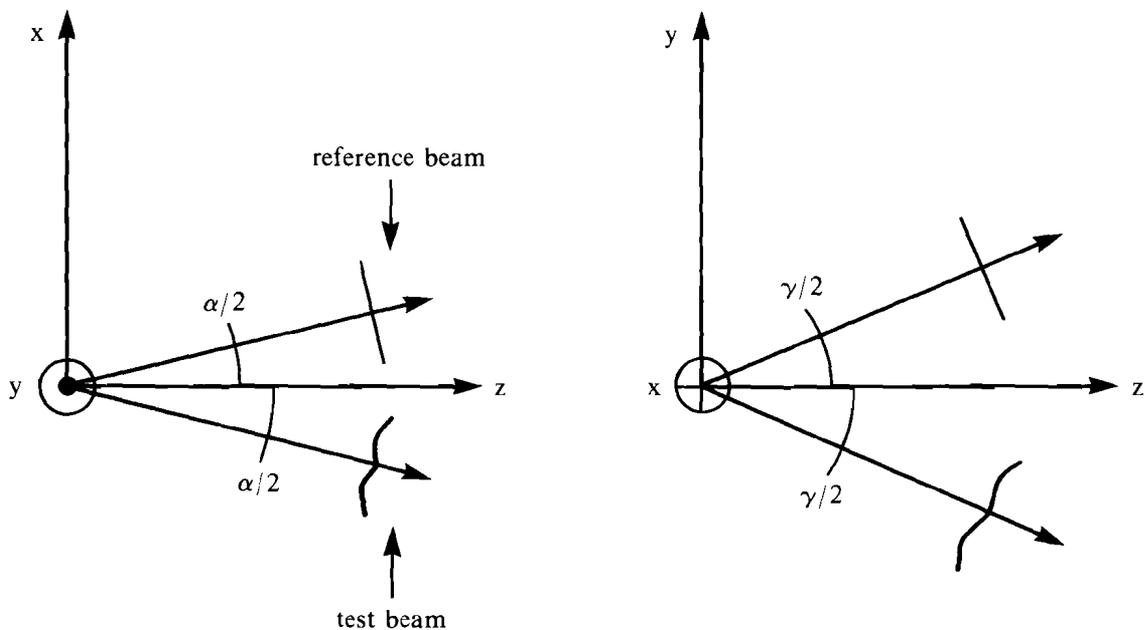
and

$$R(x,y)\cos\left[-\omega t - kx\sin(\alpha/2) - ky\sin(\gamma/2) + \phi(x,y)\right], \quad \text{(reference)} \tag{2}$$

where $T(x,y)$, $\psi(x,y)$, and $R(x,y)$, $\phi(x,y)$ represent the amplitude and phase distributions of the electric fields. The propagation constants, $\pm\ kx\sin(\alpha/2)$ and $\pm\ ky\sin(\gamma/2)$, represent symmetric interference about the x and y axes (see Fig. 31.17). The temporal frequency ω has units of radians/second. Square-law detection of the interference between the two waves produces a signal represented by

$$S(x,y) = T^2(x,y) + R^2(x,y)$$

$$+ \ \frac{T(x,y)R(x,y)}{2}\ e^{i[2kx\sin(\alpha/2)\ +\ 2ky\sin(\gamma/2)+\psi(x,y)-\phi(x,y)]}$$

$$+ \ \frac{T(x,y)R(x,y)}{2}\ e^{-i[2kx\sin(\alpha/2)\ +\ 2ky\sin(\gamma/2)+\psi(x,y)-\phi(x,y)]} \quad (3)$$

The above expression describes the linearly recorded interferogram. Complex notation of the oscillatory interference term shows holographic phase-front storage of the two wave fronts. Phase-front reconstruction is achieved through computerized image processing.

G2068

Fig. 31.17
Two-beam interferometry involves the coherent addition of a test beam and an appropriately produced, separate reference beam. The resulting interference pattern represents wavelength contours of the optical path difference between the two waves. In the case of a perfect plane-wave reference, the fringes represent wavelength contours of the aberrated test beam. Normally, a tilt component between the two beams is added to provide a carrier frequency for visual inspection or direct digitization. The values of α and γ are very small for interferometry but increase to a maximum value of π for holography.

Synchronous phase detection[1,2,3] in the spatial domain, rather than the time domain, brings interferometric analysis into the field of digital image processing. Assuming that the variations in the phase distributions, $\psi(x,y)$ and $\phi(x,y)$, are sufficiently sampled, Fourier analysis can be accurately performed on the intensity distribution $S(x,y)$. Fourier analysis is accomplished with greater ease by the substitution of the carrier-frequency parameters

$$\omega_o = 1/d_x = 2 \sin(\alpha/2)/\lambda \text{ and } \nu_o = 1/d_y = 2 \sin(\gamma/2)/\lambda$$

represented by

$$S(x,y) = T^2(x,y) + R^2(x,y)$$

$$+ \frac{T(x,y)R(x,y)}{2} e^{i[2\pi(\omega_o x + \nu_o y + \psi(x,y) - \phi(x,y)]}$$

$$+ \frac{T(x,y)R(x,y)}{2} e^{-i[2\pi(\omega_o x + \nu_o y + \psi(x,y) - \phi(x,y)]} . \quad (4)$$

The signal $S(x,y)$ is appropriately stored in the computer as a complex 2-D digital image, since an imaginary component forms during image manipulation. A complex 2-D Fourier transform of $S(x,y)$, defined as

$$F[S(x,y)] = s(\omega,\nu) \equiv \int\int_{-\infty}^{\infty} S(x,y) e^{-i2\pi(x\omega + \nu y)} dxdy , \quad (5)$$

is performed with an array-processor-enhanced, 2-D fast-Fourier-transform (FFT) algorithm. The image in the Fourier domain can be expressed as

$$s(\omega,\nu) \propto b(\omega,\nu) + t(\omega - \omega_o, \nu - \nu_o) ** r^*(\omega - \omega_o, \nu - \nu_o)$$

$$+ t^*(\omega + \omega_o, \nu + \nu_o) ** r(\omega + \omega_o, \nu + \nu_o), \quad (6)$$

where $B(x,y) \propto T^2(x,y) + R^2(x,y)$; b, r, and t represent the Fourier transform of B, R, and T respectively; * denotes complex conjugation and ** denotes a 2-D convolution. The first term $b(\omega,\nu)$ represents the "zero-order" component, or background signal. Each of the two other terms contains the relevant phase information. Fourier side-lobe filtering is performed to extract one of the phase-front terms from all of the other information. Assuming nonoverlapping Fourier components, the side lobe is extracted with a rect(ω) rect(ν) window and shifted to the origin (see Fig. 31.18). This is represented by

$$s_F (\omega,\nu) \propto \delta(\omega + \omega_o, \nu + \nu_o) ** \left\{ s(\omega,\nu) \times \text{rect}\left[\frac{\omega - \omega_o}{\Delta\omega_c} , \frac{\nu - \nu_o}{\Delta\nu_c} \right] \right\}, \quad (7)$$

where $\Delta\omega_c$ and $\Delta\nu_c$ are spectral widths of the desired side-lobe filter, centered on the carrier frequencies ω_o and ν_o. Again, using an FFT
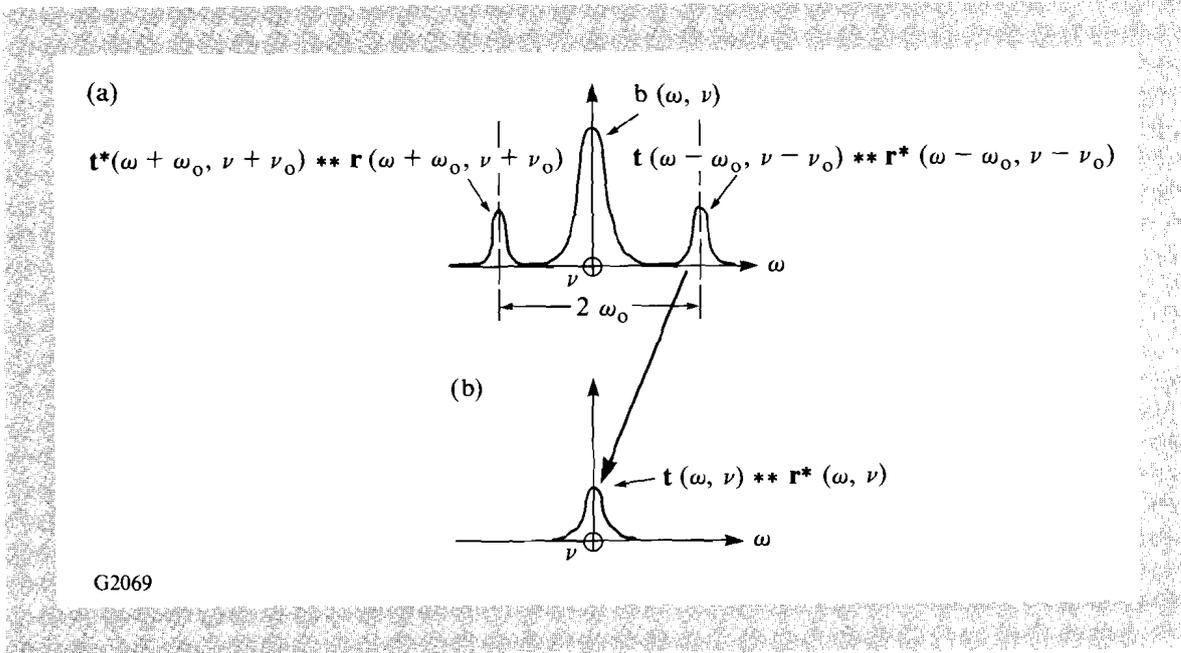
Fig. 31.18

The separated 2-D Fourier spectra (a) associated with the high-frequency interferogram. The left and right lobes both contain the required phase information and are symmetric about the origin. A window function is used to select the right lobe and shift it to the origin, thus removing all tilt from the recovered phase distribution. Experimentally, the carrier frequency is chosen to minimize overlap between the beam's power spectrum and the encoded phase.

algorithm, a reverse Fourier transform returns the analysis to the spatial domain, represented by

$$S_F \ (x,y) \ = \ \frac{T(x,y)R(x,y)}{2} \ e^{i[\psi(x,y)-\phi(x,y)]} \ . \tag{8}$$

Taking a complex logarithm yields

$$\log \ [S_F(x,y)] \ = \ \mathrm{Log} \ \left[\frac{T(x,y)R(x,y)}{2} \right] \ + \ i \left[\psi(x,y) - \phi(x,y) \ + \ 2N\pi \right] , \tag{9}$$

where the imaginary component is the recovered phase difference between the test and reference beams. Since the digital interferogram is stored as a complex image, it is necessary to calculate only an arc tangent function,

$$\psi(w,y) - \phi(x,y) \ = \ \tan^{-1} \left\{ \frac{\mathrm{Real}[S_F \ (x,y)]}{\mathrm{Im}[S_F \ (x,y)]} \right\} . \tag{10}$$

The arc tangent function subroutine operates over only the principal branch ($N=0$) with $-\pi < \theta < \pi$; thus, each pixel of the phase image is undetermined by a multiple of 2π. These discontinuities are corrected by appropriately shifting adjacent pixels by 2π.

An overlapping of the Fourier spectra of each of the background signals reduces the reconstructed phase-front accuracy. The effects of

Fourier-spectrum overlap can be reduced by locating the carrier frequency at a minimum of the background power spectrum. High-power laser-beam, phase-front analysis, approaching $\lambda/50$, has been achieved. Accuracies greater than $\lambda/100$ can be achieved by properly dealing with image discontinuities.[4]

Laser Interferometry

Uniformity measurements have been advanced by the design of a new beam-diagnostic package that includes photographic recording of the near-field and equivalent-target-plane intensity distributions, as well as phase-front measurement by self-generated reference-beam interferometry. Self-generated reference-beam interferometry involves the creation of a separate reference beam from the test beam.[5] Rewriting Eq. 8 to include the generation of a reference beam, we obtain
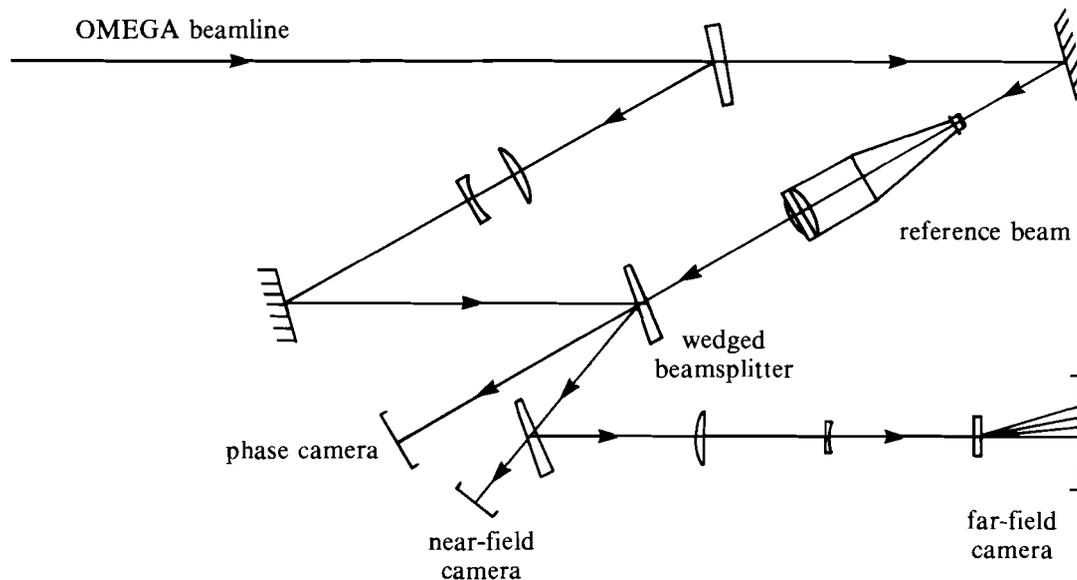
$$S_F(x,y) = \frac{T(x,y)T(xM,yM)}{2}\ e^{i[\psi(x,y)-\psi(xM,yM)]} \ . \tag{11}$$

Radial shearing interferometry is performed when the magnification M is about 1 to 10. However, as M approaches 100, two-beam interferometry can be performed. There must exist a region of the test beam over which the phase error changes by no more than the desired phase-front accuracy.

Figure 31.19 schematically illustrates the way in which two beams are produced using a parallelogram Mach-Zehnder configuration. The test beam is down collimated in one arm of the system, while a high-

Fig. 31.19
A parallelogram Mach-Zehnder interferometer, used to measure the phase front of a high-power, solid-state laser beam, includes a self-generated reference beam in one arm and a down-collimated test beam in the other. Near-normal incidence of reflection reduces the sensitivity to polarization-dependent phase fronts. The position of the reference-beam collimator is varied for spatial selection of the reference or to study coherence effects. The angle of the recombining beam splitter can be varied throughout the interferometry to holography ranges.

OMEGA beamline

reference beam

wedged
beamsplitter

phase camera
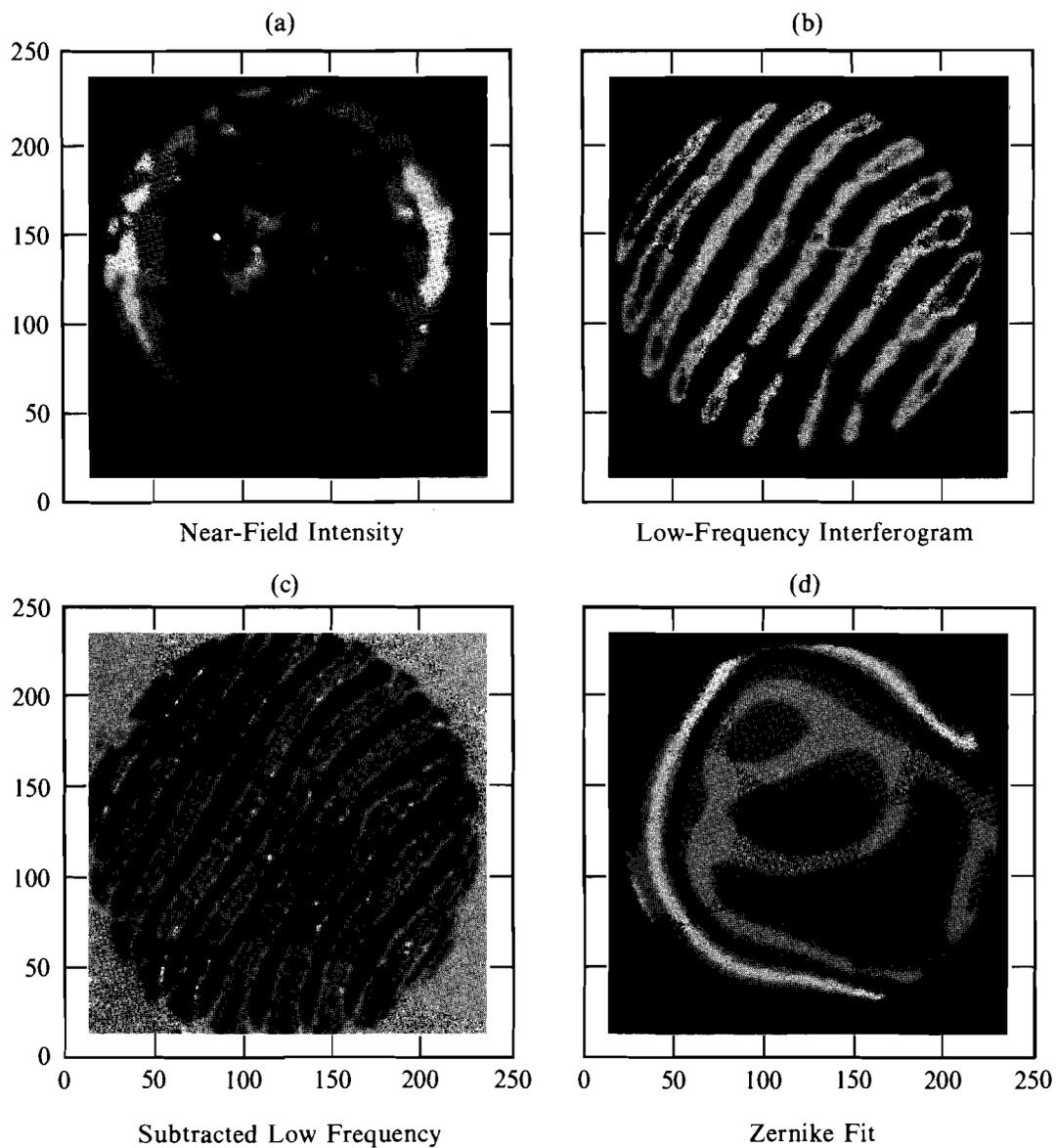
near-field
camera

far-field
camera

G1971

quality, coherent reference is created from a sufficiently small region of the transmitted test beam in the other arm. Two-beam interference is formed by the recombining beam splitter such that the fringe frequency is variable over the interferometry to holography ranges, i.e., the angle between the two wave fronts varies from 0° to 180°. Near-normal incidence is used on the two bare-surface beam splitters to prevent polarization sensitivity. Conventional photographic methods are used to record the interferometric intensity distributions.

OMEGA Phase Analysis

High-power laser interferometry and high-resolution fringe analysis have been applied to beamline 6-2 of the OMEGA laser system. Initially, interferograms were generated with a low tilt-fringe frequency, sufficient for an analysis consisting of intensity subtraction and hand digitization of the fringe contour peaks. Figure 31.20 shows the various images involved in this routine. The near-field intensity [Fig. 31.20(a)] and interferogram [Fig. 31.20(b)] were first digitized on a microdensitometer. An offset and a multiplier of the near-field intensity are subtracted from the original interferogram to provide an enhanced fringe pattern [Fig. 31.20(c)]. The fringe contour peaks are hand digitized, producing between 100 to 200 data points that are least-square fit to an eighth-order Zernike polynomial. A contour of the detected phase is shown in Fig. 31.20(d). Hand digitization and analysis were repeated to demonstrate a reproducibility of approximately $\lambda/15$. However, $\lambda/15$ accuracy and a few-hundred-point resolution did not account for the intensity modulations that were observed with UV equivalent-target-plane photography.

Phase-front measurements of beamline 6-2 were repeated with spatial synchronous phase detection. Figure 31.21 is a flow chart describing the image manipulation of the high-frequency interferogram. A measurement accuracy of $\lambda/50$ over an image area of 256 × 256 pixels was achieved. With this measurement, diffraction modeling, involving computerized beam propagation of the near-field amplitude and phase distributions, established that the irradiation uniformity level on target is dominated by the phase front of the individual beams. In particular, the high-frequency components were responsible for most of the nonuniformity (see the article in this issue entitled "A Source of Hot Spots in Frequency-Tripled Laser Light"). Interferometric analysis of the pulsed-laser radiation and the individual components of a beamline has identified the major sources of phase modulation. Practical limitations on the homogeneity of glass and crystals and on surface figuring indicate that all optical elements contribute phase errors to a laser beamline. It is the 2-D accumulation of these phase errors, from large numbers of optical elements, that statistically degrades the beam's phase front. In addition, the reproducibility of the phase front is affected by dynamic sources of phase modulation, such as atmospheric turbulence and pump-induced amplifier stress.
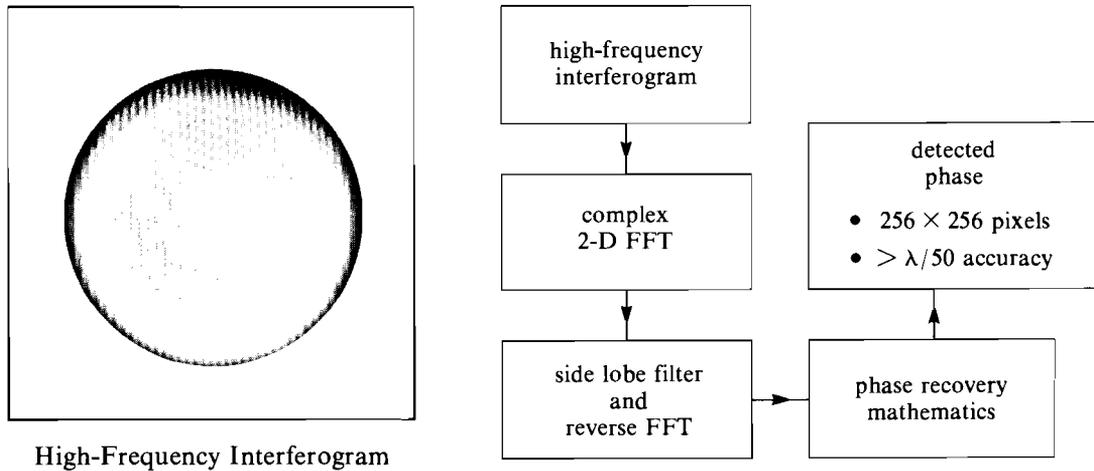
The major thrust in the areas of phase-front measurements and improvements to the OMEGA laser involves distinguishing the reproducible and irreproducible components of the phase front. Figure 31.22 shows preliminary results of high-resolution phase

(a)

Near-Field Intensity

(b)

Low-Frequency Interferogram

(c)

Subtracted Low Frequency
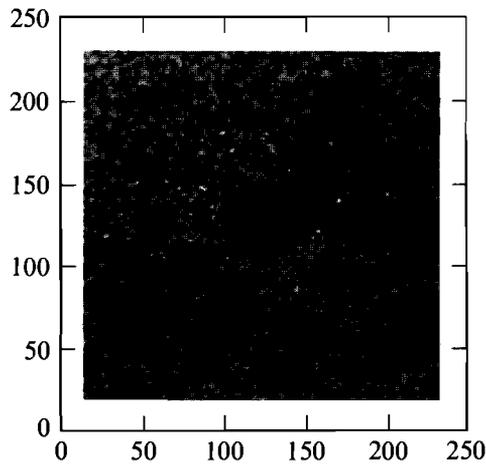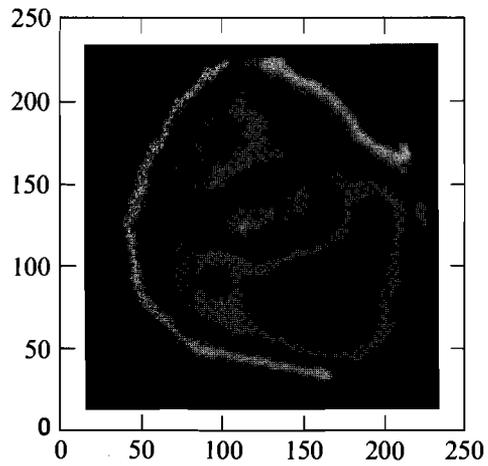
(d)

Zernike Fit

G2070

Fig. 31.20
For visual inspection or hand digitization of the contour peaks, a tilt component corresponding to a dozen fringes over the beam diameter is selected (b). The phase front of the beam is encoded within the fringe contours of the interferogram. Enhanced fringes (c) are obtained by subtracting the near-field intensity (a) from the original interferogram. Hand digitization of the contour peaks is followed by an eighth-order Zernike-polynomial least-squares fit to the data points. Repeated digitization and analysis have indicated an accuracy of approximately $\lambda/15$. Smooth contours of phase (d) are an indication of the bandpass limit associated with an eighth-order polynomial fit to hand-digitized data.

High-Frequency Interferogram

high-frequency
interferogram

complex
2-D FFT

side lobe filter
and
reverse FFT

phase recovery
mathematics

detected
phase
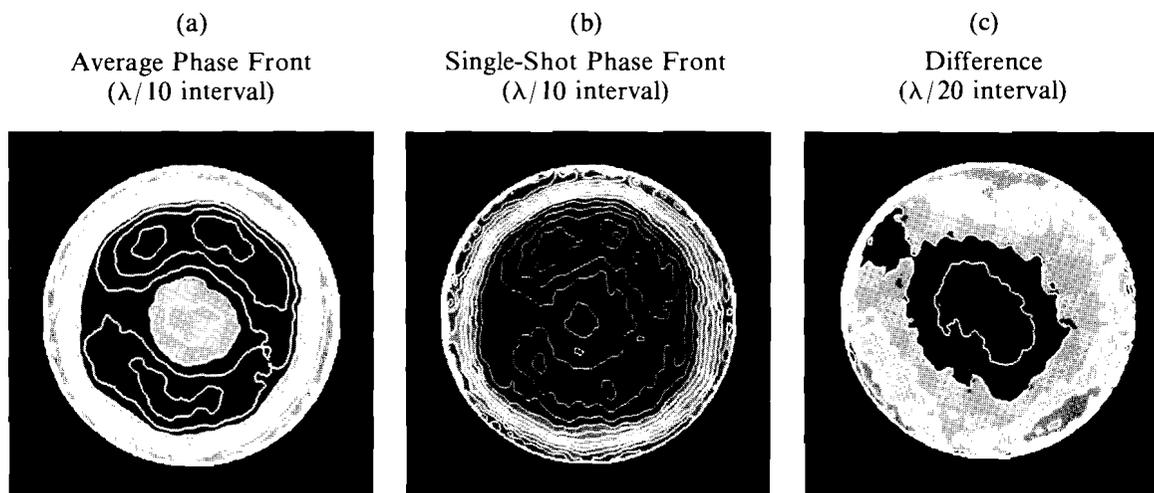• 256 × 256 pixels
• > λ/50 accuracy

2-D FFT of Interferogram

Detected Phase
(λ/7 contour level)

G1979

Figure 31.21
Spatial synchronous phase detection (SSPD) makes possible the application of phase-shifting interferometry to high-power pulsed radiation. A large tilt is introduced between the test and reference beams to produce a high-frequency interferogram. Fourier analysis of this complex image provides a method for eliminating the amplitude errors associated with direct-fringe digitization. SSPD offers a measurement accuracy of greater than λ/50 over an image area of 256 × 256 pixels. The detected phase (lower right) shows the high-frequency phase information that is recovered from SSPD analysis. Comparison with Fig. 31.20 shows the increased phase bandpass. Subsequent modeling showed that phase features as small as λ/30 (λ = 1.054 μm) are responsible for intensity nonuniformities on target.

(a)
Average Phase Front
($\lambda/10$ interval)

(b)
Single-Shot Phase Front
($\lambda/10$ interval)

(c)
Difference
($\lambda/20$ interval)

G2028

Figure 31.22
Phase-front reproducibility is essential for static phase correction. The difference (c) between a single driver-line shot (b) and an average of six shots (a) is substantially lower in phase distortion than for any one shot. Reproducibility can be increased through amplifier development and turbulence control.

measurement of the driver line. A large reproducible component of the phase front indicates that phase-correction technologies can improve driver-line performance. Once the irreproducible phase effects are reduced or eliminated, the feasibility of phase correction strategies can be fully assessed. Conventional glass phase plates and holographic corrector elements are currently under investigation. In addition, spatial filtering experiments are being conducted to determine the practical limits of eliminating the high-frequency phase components.

Future Applications
High-power laser interferometry will be applied to all of the OMEGA beamlines following diagnostic development and improvements to the synchronous-detection algorithms. This powerful tool will also aid in the characterization of cryogenic-target fuel layers. Time-dependent phase effects in lasers and laser amplifiers can be studied with electronic spatial-synchronous phase detection. Furthermore, filamentation studies of underdense plasmas, using an optical probe, can be enhanced with high-resolution interferometry.[6]

Summary
Self-generated reference beam interferometry has been successfully implemented on an OMEGA high-power laser beam. Spatial-synchronous phase detection is an image-processing-based analysis technique that provides high-resolution phase-front reconstruction. Together, these developments make it possible to perform phase-shifting interferometry on high-power pulsed radiation. Furthermore, with this measurement technique, diffraction modeling has provided a